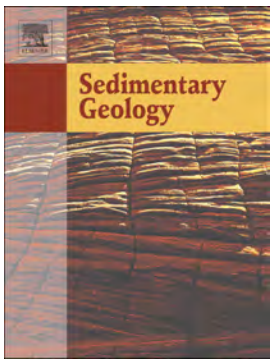


# Evidence of cyclic climatic changes recorded in clay mineral assemblages from a continental paleocene-eocene sequence, northwestern Argentina

Margarita Do Campo, Blanca Bauluz, Cecilia Del Papa, Timothy White, Alfonso Yuste, Maria Jose Mayayo

PII: S0037-0738(18)30047-2
DOI: doi:10.1016/j.sedgeo.2018.03.007
Reference: SEDGEO 5323

To appear in:

Received date: 29 December 2017
Revised date: 7 March 2018
Accepted date: 9 March 2018

Please cite this article as: Margarita Do Campo, Blanca Bauluz, Cecilia Del Papa, Timothy White, Alfonso Yuste, Maria Jose Mayayo , Evidence of cyclic climatic changes recorded in clay mineral assemblages from a continental paleocene-eocene sequence, northwestern Argentina. The address for the corresponding author was captured as affiliation for all authors. Please check if appropriate. Sedgeo(2018), doi:10.1016/j.sedgeo.2018.03.007

# EVIDENCE OF CYCLIC CLIMATIC CHANGES RECORDED IN CLAY MINERAL ASSEMBLAGES FROM A CONTINENTAL PALEOCENE-EOCENE SEQUENCE, NORTHWESTERN ARGENTINA

MARGARITA DO CAMPO[a], BLANCA BAULUZ[b], CECILIA DEL PAPA[c], TIMOTHY WHITE[d], ALFONSO YUSTE[b], MARIA JOSE MAYAYO[b]

[a] Universidad de Buenos Aires and INGEIS (CONICET – UBA), Ciudad Universitaria, Intendente Güiraldes s/n (1428) Buenos Aires, Argentina. Email: docampo@ingeis.uba.ar

[b] IUCA-Departamento de Ciencias de la Tierra, Universidad de Zaragoza, Pedro Cerbuna 12, (500009) Zaragoza, Spain. Email: bauluz@unizar.es

[c] CICTERRA, CONICET-Universidad Nacional de Córdoba, Av. Vélez Sarsfield 1699, X5016GCB Córdoba, Argentina. Email: delpapacecilia@yahoo.com

[d] Earth and Environmental Systems Institute, The Pennsylvania State University, PA 16802, USA. Email: tsw113@psu.edu



## ABSTRACT

The continental Paleocene-Eocene sequence investigated in this study belongs to the Salta Group, deposited in an intracontinental rift, the Salta Basin (NW Argentina), that evolved from the lower Cretaceous to the middle Paleogene, and is subdivided into the Pirgua, the Balbuena and the Santa Barbara Subgroups. The Maíz Gordo Formation (200 m thick) is the middle unit of the Santa Bárbara Subgroup, deposited during late post-rift sedimentation. We studied the mineralogy of fine-grained horizons of this formation by X-ray diffraction and Scanning Electron Microscopy (SEM) in order to examine the connection between vertical changes in clay mineralogy in alluvial sediments and paleosols, and global paleoclimatic changes registered during the Paleogene. Paleosols vary from calcic vertisols in the lowermost levels, to inseptisols and gleysols in

intermediate positions, to gleyed oxisols in the upper section, indicating increased chemical weathering through time.

Clay mineral relative abundances vary with a general increase in kaolinite content from bottom to top. However, at one site there are significant variations in kaolinite/muscovite (Kln/Ms) that define five cycles of kaolinite abundance and Kln/Ms that indicate cyclic patterns of paleoprecipitation and paleotemperature. These are interpreted as several short-lived hyperthermals during the Paleocene-early Eocene in the Southern Hemisphere, which correlate with well-established episodes of warmth documented from the Northern Hemisphere.

**KEYWORDS:** Paleoclimate reconstruction, continental basins, Kaolinite, paleosols, clay minerals

## 1. INTRODUCTION

The study of continental paleoclimates is crucial for the understanding of global climate patterns and also required for the development of predictive climate models. Clay minerals are considered good paleoclimatic proxies because their genesis in the sedimentary realm is strongly controlled by weathering intensity that in turn is controlled by paleoclimatic conditions. Physical weathering prevails under dry and cold climates, giving way to clay mineral assemblages dominated by illite and/or chlorite. On the other hand, under warm climate conditions with alternating humid and dry seasons when chemical weathering is reasonably mild or slow, smectite can form (Buurman et al., 1988; Güven, 1988; Chamley, 1989; Murakami et al., 1996). In contrast, under humid subtropical to tropical climates, highly hydrolytic conditions prevail, leading to the formation of laterites, lateritic clays, and bauxites, where kaolinite is the main clay mineral (Chamley, 1989; Righi and Meunier, 1995). In those cases, kaolinite usually forms through the dissolution of aluminosilicates such as feldspars or micas in the presence of water. This reaction is enhanced by high temperatures and low pH. The contrasting climatic conditions that favor illite

and kaolinite genesis in weathering profiles led Chamley (1989) to propose the kaolinite/mica ratio (Kln/Ms), calculated from their relative abundances, as a paleoclimate proxy. Several studies based on variation of clay mineral assemblages in continental sequences and paleosols have been of great interest in order to infer paleoclimatic and paleoenvironmental conditions in Mesozoic and Cenozoic strata (e.g., Ruffell et al., 2002; Raucskik and Varga, 2008; Bauluz et al., 2014, and references therein).

The early Cenozoic is characterized by a series of short-lived hyperthermals, the largest of these being the Paleocene-Eocene Thermal Maximum (PETM), considered to have been the warmest period of the Cenozoic Era (Kennett and Stott, 1991; Zachos et al., 1993, 2001; Schmitz and Pujalte, 2007; Sluijs et al., 2007; McInerney and Wing, 2011). The PETM occurred ~56 million years ago in a short period of time that spanned ~170,000 years (Röhl et al., 2007; Westerhold, 2008; Charles et al., 2011; Zeebe et al., 2016) and many researchers consider it to be a good analog for ongoing climate change, as the calculated rate and amount of carbon released to the atmosphere during the PETM could be similar to ongoing anthropogenic releases (Zeebe et al., 2016). During this event, a pronounced global warming of ~5 °C of the oceans and atmosphere took place (e.g., Kennett and Stott, 1991; Koch et al., 1992; Zachos et al., 2003, 2005; Tripati and Elederfield, 2005; Sluijs et al., 2006; Röhl et al., 2007). On the other hand, the effect of PETM warming on the paleohydrological cycle is less straightforward. The results obtained in different continental basins indicate that the PETM was characterized by enhanced seasonal precipitation (Schmitz and Pujalte, 2007; Domingo et al., 2009; Baczynski et al., 2017), but in other basins like the Bighorn Basin, Wyoming, this period is associated with intervals of wetness/dryness (Kraus and Riggins, 2007).

A number of studies of the PETM focused on the temperature variation in the oceans mainly from the study of deep-sea cores (e.g., Kennett and Stott, 1991; Tripati and Elderfield, 2005; Zachos et al., 2005, 2010; Sluijs et al., 2006). On the other hand, fewer studies have focused on terrestrial sections and those that have been accomplished are mostly in the Northern

Hemisphere in the United States and Europe (Koch et al., 2003; Kraus and Riggins, 2007; Schmitz and Pujalte, 2007; Domingo et al., 2009). These studies have applied different approaches to understand environmental conditions that prevailed during the PETM, including the use of carbon and oxygen isotope data, and sedimentological features (Koch et al., 1995, 2003; Schmitz and Pujalte, 2007; Domingo et al., 2009).

Studies of sediments spanning the PETM have detected a shift from smectite to dominantly kaolinite in the clay fraction of paleosols in several localities in the Northern Hemisphere, interpreted as increased weathering due to increased temperature and humidity during this hyperthermal event (Robert and Kennett, 1994; Clechenko et al., 2007; White and Schiebout, 2008).

Despite the paleoclimatic reconstructions in Paleocene-Eocene continental materials, only a few have been carried out in the Southern Hemisphere. The recent study by Andrews et al. (2017) focused on paleosols from the Santa Barbara Subgroup in the western part of the Salta Basin, northern Argentina, which include strata spanning the PETM. These authors deduced increased mean annual paleoprecipitation of ~1500 mm and paleotemperature of ~ 5 °C at the height of the PETM. Based on organic matter carbon isotope data, Andrews et al. (2017) identified a ~-6‰ carbon isotope excursion (CIE) that they interpret as a record of the PETM at the top of the Maíz Gordo Formation (Fm), plus two other CIEs of lesser magnitude. However, they could not isotopically characterize the whole unit due to the lack of appropriate lithologies for analyses.

The objective of the present study is to infer the textural relations and origin of clays in the Maíz Gordo Fm in the western part of the Salta Basin (northwestern Argentina) and to correlate clay mineral assemblage variations with possible changes in weathering intensity due to paleoclimate changes during the Paleocene-Eocene. A secondary goal is to compare the efficacy of clay mineralogy for paleoenvironmental reconstruction to other well established paleoclimate indicators, such as carbon isotope data in carbonates and organic matter and chemical weathering indices used in previous studies (Andrews et al., 2017, and references therein).

## 2. METHODS AND SAMPLES

We measured and described bed by bed three selected sites: Obelisco located on the outskirts of Cafayate, and Tin Tin and Tonco located in the Parque Nacional Los Cardones (Fig. 1) to study the changes of clay mineral associations in paleo fluvial environments. Each site was sampled taking into account sedimentary facies and paleosol types of the Maíz Gordo Fm as described in Andrews et al. (2017), and a few meters of the underling Mealla and overlying Lumbrera formations. At Tin Tin and Tonco the whole Maíz Gordo Fm was sampled, whereas at Obelisco the intermediate levels are coarse grained and thus are not useful for a clay minerals study. Moreover, the Tin Tin and Obelisco sections are the same as those reported in Andrews et al. (2017).

The mineralogical composition of 45 whole rock and clay sub-samples (26 from Tin Tin, 9 from Obelisco and 10 from Tonco) of the Maíz Gordo Fm were analyzed by X-ray diffraction (XRD). Moreover, 17 samples from the Mealla and Lumbrera formations (11 from Tin Tin, 4 from Obelisco and 2 from Tonco) were also analyzed by XRD in order to identify changes in clay mineralogy between units. The distribution of the samples along the Tin Tin stratigraphic log is shown in Figure 2A. XRD analysis was performed with a Philips PW 1710 diffractometer scanning with Cu-K$\alpha$ radiation, an automatic divergence slit and a graphite monochromator working with 40Kv and 40mA. The XRD patterns were recorded from 3° to 30° 2$\theta$, with a scan rate of 0.1° 2$\theta$/sec and integration time of 0.4 sec.

The XRD data were stored as computer files with the XPowder software (Martin, 2004). The analysis comprises whole rocks and <2-µm sub fractions. Clay sub-samples (<2 µm) were prepared in accordance with the guidelines of Moore and Reynolds (1997). The mineral intensity factors (MIF) of Moore and Reynolds (1997) were employed to estimate the relative abundances of illite-mica, kaolinite, smectite and I/S mixed-layer clays. The ratio of kaolinite and illite-mica (Kln/Ms) abundances was then calculated.

We performed standard petrographic analyses to determine lithology and textural features of the samples corresponding to the three study sections. Afterwards, seven samples characterized by their high kaolinite content were chosen for detailed study using Field Scanning Electron Microscopy (FESEM) employing a Carl Zeiss FESEM to obtain textural and chemical information of the clay minerals at micro and nanoscale. First, fragments of the samples were studied using secondary electron (SE) images employing an accelerating voltage of 5Kv with a beam current of 100 pA. In the case of the back-scattered electron study (BSE) and the X-ray dispersive (EDS) analysis, polished thin sections were employed. The accelerating voltage used was 15Kv with a beam current of 1 nA. Atomic concentration ratios obtained by EDS were converted into formulae according to stoichiometry. Accordingly, the structural formulae of dioctahedral smectite were calculated on the basis of 22 negative charges ($O_{10}(OH)_2$).

**3. GEOLOGICAL SETTING**

An intra-continental rift basin – Salta Basin – was developed in northwestern Argentina during Cretaceous-Eocene times (Salfity and Marquillas, 1994; Viramonte et al., 1999). The Salta Group mostly comprises continental sediment interrupted by a marine incursion during the Cretaceous-Paleogene transition (Marquillas et al., 2005). Deposition of the Maíz Gordo Fm took place during thermal subsidence in the post-rift stage. This unit constitutes, along with the Mealla and Lumbrera formations, the Santa Bárbara Subgroup, that comprises fluvial environments in proximal areas and lakes in the center of the basin (for details, see del Papa and Salfity, 1999).

In the fluvial environment, the Mealla Fm consists of fine-grained conglomerates to medium sandstones and thick mudstones interpreted as perennial braided to high sinuosity down-system fluvial environments, and is typically 150-200 m thick (del Papa and Salfity, 1999).

The Maíz Gordo Fm was characterized by sedimentation in and near a brackish-alkaline lake with a ramp-type margin surrounded by a braided fluvial setting (del Papa, 1999). The fluvial

environment shows a continuous grain-size gradation from proximal conglomerates to distal sandy facies in the transition to lacustrine strata (del Papa and Salfity, 1999). In the study area, thickness of the Maíz Gordo Fm ranges from 113 m in the Tin Tin section to 178 m in the Tonco section, and is in paraconformable contact with the underlying Mealla and overlying Lumbrera formations (Fig. 2).

The Lumbrera Fm is 200m thick and consists of thick sandy mudstones and coarse-grained sandstones deposited in meandering fluvial settings (del Papa and Salfity, 1999).

Until recently, age constraints on the units integrating the Salta Group were based on biostratigraphic and palynostratigraphic studies. Land mammal associations and palynostratigraphy of the Santa Bárbara Subgroup indicate that the Mealla and Maíz Gordo formations date to the Selandian and Thanetian respectively; the final two ages of the Paleocene Epoch. The Lumbrera Fm has been dated using land mammal associations and palynostratigraphy to the Eocene (Quattrocchio et al., 2005; del Papa et al., 2010). Additionally, in the upper ~30 m of the Maíz Gordo Fm comprising a thick prominent paleosol section, Andrews et al. (2017) obtained organic matter carbon isotope data ranging from -22‰ to ~-28‰, used to interpret this interval as spanning the Paleocene-Eocene. A recent study carried on in nearby coeval sections applied paleomagnetic results to constrain the age of the Mealla Fm from 59.4–58.9 Ma in the mid Paleocene (Hyland et al., 2015), in agreement with palynostratigraphic age determinations. The site studied by Hyland et al. (2015) lies between the sites presented here (Cerro Bayo in Fig. 1A), so the paleomagnetic data provided by these authors allow some age constraints for our study sections. However, in a further study at the same locality, Hyland et al. (2017) assigned an age of ~ 53.5 Ma to the top of the Mealla Fm, thus setting the bottom of the Maíz Gordo Fm in the Ypresian, the first stage of the Eocene Epoch. In reply to a comment from Hyland and Sheldon (2017), White et al. (2017) have questioned the foundation of the Hyland et al. (2017) approach to constraining their magnetostratigraphic record and therefore the age model they proposed.

Thus, in the absence of absolute radiometric determinations, the age of the Maíz Gordo Fm is still not well constrained.

The present study is focused on the coarse-proximal fluvial setting of the Maíz Gordo Fm, mainly considering the fine-grained lithologies of the paleofloodplain that contain abundant well-developed paleosols (Fig. 1).

## 4. SEDIMENTARY FACIES OF THE MAÍZ GORDO FORMATION

The sedimentary facies associations recognized in the study area are typified as i) gravelly to sandy channels, and ii) sandy siltstone floodplain deposits. The channel facies association (CH) consists of 2-7 m of tabular bodies composed of stacked single beds of white to gray, granular conglomerate to coarse-grained sandstones. Each bed is highly lenticular to shallow lenticular, with concave-up scour bases and lag deposits of pebbles to cobbles. Normal grading, parallel stratification and trough cross–bedding are the common sedimentary structures (Fig. 3A); also some bed tops are clay rich with root traces and carbonate nodules.

The floodplain facies association (OF), is of variable thickness from 3 m to only a few cm sandwiched between channels (Fig. 3B), and is composed of granule/sandy siltstones or mudstones, where the larger clasts are floating in the fine-grained material. The color changes from reddish-brown in the lower section to dark gray and purple in the upper section (Fig. 2). Most of the fine-grained horizons are poorly stratified, massive or altered by pedogenesis. In the latter case they display carbonate/Fe-oxide nodules, root traces, rhizoconcretions and mottling. Also the ant nest trace fossil *Krausichnussisi* (Genise et al., 2016) has been recognized related to paleosols in the lower part of the unit. This particular ant nest forms a complex pedotubule network and has been interpreted as having formed in fluvial valleys with nearby dry woodlands (Genise et al., 2016). Interlayered with the fine-grained sediments are thin, highly lenticular granulitic conglomerates, displaying pedogenic features.

These facies associations are consistent with rivers dominated by bedload, with multiple channels typical of braided systems. Moreover, the persistence of coarse-grained strata both in channels and the floodplains, and the low relief of the architectural elements suggest that most of the floodplain was built up by the shifting of a channel belt that, after abandonment, was colonized by biota (Rust, 1972; Nanson and Croke, 1992). This scheme also suggests that unstable channels and high frequency avulsion events led to braidplain aggradation (e.g., Hajek and Wolinsky, 2012). Braidplains are frequently developed under humid climates (Nichols, 2009) where the high availability of water and sediment contributes to multi-channeling and braiding (Bridge, 2003).

**5. PALEOSOL DESCRIPTION**

The Maíz Gordo Fm is comprised of amalgamated stacks of polygenetic paleosols developed mainly in floodplain facies that are principally white to light gray clayey coarse sandstone to sandy mudstones (Andrews et al., 2017). Moreover some channel tops also display some degree of pedogenesis. The distribution of paleosol types along the stratigraphic column is sketched in Fig. 2B.

Paleosols in the lower section of the formation show isolated vertic features, carbonate pedotubules, reddish brown mottles and carbonate nodules, suggesting the presence of calcic vertisols. Upsection the carbonate nodules disappear and instead clay slickensides, iron-rich concretions and redoximorphic features are present, typical of inseptisols and gleysols. At the top of the unit an ~30 m section is characterized by abundant vertical and horizontal reddish brown and yellow pedotubule networks in a white to light gray matrix of clayey sandstone. Greenish-gray redoximorphic features are visible in places and no clay slickensides were observed. A prominent greenish gray clayey sandstone with abundant red to blue to purple reticulate hematite/siderite nodules, blocky peds and pedotubules, suggesting gleyed oxisols (Fig. 3B, D) exists at the top of the formation. The upsection change in paleosol types suggests a progressive increase in chemical

weathering perhaps through changes to warmer and wetter conditions. The upper section corresponds to nearby coeval highstand lacustrine deposits (del Papa, 1999). The underlying Mealla Fm consists of white fine to coarse/pebbly sandstones interbedded with thick (3-10 m) red clayey siltstones on which calcic paleosols developed (Fig. 3C). The overlying Lumbrera Fm consists of grayish red coarse-grained sandstones in lenticular channel forms interbedded with dark red sandy mudstone on which calcic paleosols formed (Andrews et al., 2017).

**6. MINERALOGY: X-ray diffraction (XRD)**

Forty five whole rock and clay sub-samples (26 from Tin Tin, 9 from Obelisco and 10 from Tonco) of the Maíz Gordo Fm were analyzed by XRD. For comparison seventeen samples from Mealla and Lumbrera formations (11 from Tin Tin, 4 from Obelisco and 2 from Tonco) were also sampled and analyzed in order to characterize the mineralogical variations through the profiles. At Tin Tin and Tonco, sampling covered the whole Maíz Gordo Fm. In contrast, at Obelisco the intermediate levels were not sampled as they are coarse grained and thus unsuitable for clay minerals analysis. The stratigraphic position of the samples corresponding to the Tin Tin section is shown in Figure 2A. The results are summarized in Tables 1 and 2.

**6.1 Whole rock mineralogy**

XRD analysis of bulk samples of the claystones, siltstones and fine-grained sandstones shows quartz and phyllosilicates as the major components in association with plagioclase, K feldspar and carbonates. Feldspars contents (K feldspar + plagioclase) are usually low in most of the samples (< 15%). Some samples of the Maíz Gordo Fm do not contain plagioclase. Calcite is mostly absent in Maíz Gordo Fm samples, whereas it was detected in several levels from the Mealla and Lumbrera formations in variable amounts from traces up to 31%. Hematite is frequently present in subordinate amounts in beds from all three formations at Obelisco and in the Mealla Fm at Tin Tin. At Obelisco several levels from the Maíz Gordo Fm contain analcime, in one case in

association with halite. Moreover, at Tin Tin a horizon from the top of the Maíz Gordo Fm contains minor gypsum.

**6.2 Clay Mineralogy**

Clay-mineral assemblages identified in the top levels of the Mealla Fm at the base of the study section at Obelisco and Tin Tin sites are commonly dominated by illite-mica with subordinate smectite (Tables 1, 2). However, one white fine sandstone level containing a clay assemblage dominated by smectite with scarce kaolinite and illite-mica was identified at Tin Tin (Table 1).

The Maíz Gordo Fm depicts significant changes in kaolinite (0-82%) and illite-mica (16-93%) relative abundances, whereas smectite is, with few exceptions, a subordinate component of the clay fraction and consequently shows less variation (0-38%) (Tables 1, 2).

At Tin Tin a general trend of increase in kaolinite relative contents from bottom to the top is observed, although superimposed with significant fluctuation in its abundance that lead us to define five cycles that are described below (Fig. 2C).

In the base of the Maíz Gordo Fm at Tin Tin, illite-mica is very abundant whereas the relative abundance of smectite is ~20% and kaolinite is absent, thus depicting a Kln/Ms of 0. A sharp increase in kaolinite content is encountered 25 m upsection together with an abrupt decrease in smectite and illite-mica relative abundances and a Kln/Ms of 0.68 (Table 1). Kaolinite relative abundances gradually increase upwards at the expense of illite-mica for the next 50 m(sample MG-T10), except for slight fluctuations, reaching a maximum Kln/Ms of 1.3. Then, kaolinite contents and the Kln/Ms decrease to 0.8 in 5 m in the section. These ~ 70 m of the Maíz Gordo Fm at Tin Tin constitute what we define as cycle I, comprising the material from the bottom of the Maíz Gordo Fm without kaolinite up to the levels in which kaolinite prevails over illite-mica (Kln/Ms = 1.3) and then those depicting a new decrease in the Kln/Ms (0.80). Towards the top of the unit, four more cycles of varying kaolinite relative abundances occur in shorter intervals,

depicting maximum Kln/Ms of 2.7, 5.2, 3.9 and 3.3, respectively (cycles II, III, IV and V) (Table 1). Each cycle implies an increase and a subsequent decrease in kaolinite abundance (in comparison with illite-mica). On the other hand, the smectite contents remain low in the Maíz Gordo Fm at Tin Tin, except for one bed with a peak value of 38% (MGT-18) (Fig. 2C).

At Obelisco and Tonco the clay assemblages in the Maíz Gordo Fm show a similar trend as at Tin Tin. Kaolinite is absent at the bottom of the unit and increases progressively up to Kln/Ms of 2.3 at Obelisco and 2.8 at Tonco (Table 2A, B). Moreover, at Tonco another Kln/Ms peak value of 3.6 is recorded at the top of the unit. Likewise, at Obelisco smectite contents remain <10% with the exception of a horizon in which smectite has a peak value of 29%; at Tonco several levels show smectite contents around 20%.

In general, the basal portions of the Lumbrera Fm depict markedly lower kaolinite contents and Kln/Ms than the top of Maíz Gordo Fm, with illite-mica as the most abundant clay mineral. At Tonco the clay mineral assemblages contain less illite-mica and more kaolinite than at Tin Tin and Obelisco (Table 2). On the other hand, at Tin Tin there is one level in this unit that displays a remarkably higher smectite relative abundance, subordinate illite-mica and minor kaolinite (LUT-29a).

## 7. TEXTURAL STUDY: Optical and Field Scanning Electron microscopy

The samples selected for the textural study are characterized primarily by their high kaolinite content, with subordinate illite and minor smectite. Six samples are distributed through the Tin Tin section and the others are from Obelisco (Tables 1, 2).

Secondary electron (SE) imagery of clays shows characteristic morphologies that allow for their identification. Smectite shows its typical morphology as “cornflakes” and kaolinite occurs as nanometer-sized sub-euhedral plates. Very scarce acicular aluminium hydroxides, probably gibbsite, have been observed in some of the samples. In contrast, illite and micas show anhedral

plates reflecting their detrital origin. Representative SE images of these phases are shown in Fig. 4.

Back scattered electron (BSE) images of samples corresponding to the middle portions of the stratigraphic section, that are characterized by medium kaolinite contents (MGT-10 and MGT-14) and Kln/Ms of 1.3 and 1.1, respectively, show heterometric and heterogeneous textures with abundant detrital fragments mainly composed of quartz, K feldspar, albite, mica and mica/kaolinite intergrowths with a matrix composed of abundant clays, smectite and kaolinite (Fig. 5A, B). Smectite displays its typical morphology as flakes and can appear between the open layers of mica/kaolinite intergrowhts, whereas kaolinite shows typical platy morphology forming booklets (Fig. 5B, C). Kaolinite and smectite, are also observed having replaced K feldspar and albite fragments (Fig. 5D). In this situation, smectite shows a curved lens-shaped morphology with no preferred orientation and kaolinite shows typical platy morphology. Smectite packets exhibit a curved lens-shaped morphology with no preferred orientation, whereas kaolinite shows typical platy morphology. Smectite forms the matrix (Fig. 5B, D) and also displays its typical morphology as flakes (Fig. 5D). Samples from the upper stratigraphic levels with higher kaolinite contents (MGT-21, 22, 24), and Kln/Ms of 2.7, 5.2 and 1.5, respectively, show similar textural features to those described for MGT- 10 and MGT- 14. However, in these cases subangular blocky peds to granules (Bullock et al., 1985) were observed, suggesting more intense pedogenesis than in the lower levels described above. Smectite packets exhibit the characteristic curved lens-shaped morphology, with no preferred orientation, whereas kaolinite shows the typical platy morphology forming booklets (Figs. 6, 7). In these samples, feldspar fragments are also intensively altered and replaced by kaolinite and smectite (Figs. 6A, 7A). These samples have abundant clay-rich matrix that consists of smectite and kaolinite-filled pores (Fig. 6B). Smectite sometimes occurs in the matrix closely associated with Fe and Ti oxides (Fig. 7G). Kaolinite plates form well-developed booklets that indicate an authigenic origin; moreover, packets of smectite are observed

surrounding the kaolinite booklets suggesting that it was formed later than kaolinite (Figs. 6B, 7D-F). Apart from smectite the matrix contains micron-sized quartz and feldspars fragments with irregular outlines suggestive of dissolution (Fig. 6C).

**8. CHEMICAL COMPOSITION OF SMECTITE-TYPE CLAYS: X–ray dispersive analysis (EDS)**

EDS analyses taken in the FESEM reflect the occurrence of abundant K-rich 2:1 clays that have replaced feldspars and form the matrix (Appendix A). These are dioctahedral clays with octahedral Al ($Al^{VI}$) higher than (Fe + Mg + Ti), whereas interlayer sites are occupied by K>Ca>Na.

In agreement with XRD data, analyses of samples MGT-22 and MGT-24 depict dioctahedral smectite, that according to the distribution of the tetrahedral and octahedral charges correspond to beidellite. On average, the clays in samples MGT-7, MGT-10 and MGT-14 have larger K contents (and interlayer charge) than those of samples MGT-22 and MGT-24 (Fig. 8A, B). Dioctahedral clays in samples MGT-7, MGT-10 and MGT-14 show broader variations in composition than those of MGT-22 and MGT-24 (Fig. 8A, B), covering the range from smectite to I/S to illite compositions. The XRD data show the presence of smectite and illite but not of I/S, thus some of the analyses probably correspond to mixtures of illite and smectite. The negative correlation between the Al and Si content in the structure of these clays is evident (Fig. 8C); this graph also shows that clays from samples MGT-22 and MGT-24 depict higher Si contents than those of MGT-7, MGT-10 and MGT-14. Fig. 8D shows a weak positive correlation between Mg and Si contents in the structure of these dioctahedral smectites.

**9. DISCUSSION**

Paleosols from the Maíz Gordo Fm vary from calcic vertisols in the lowermost levels to inseptisols and gleysols in intermediate positions to gleyed oxisols in the upper section (Fig. 2). This variation indicates increased chemical weathering through the unit. In the upper section,

Andrews et al. (2017) calculated Chemical Index of Alteration values (CIA) greater than 80 with some approaching 100, in agreement with these pedotypes. From a mineralogical point of view, the paleosols are characterized by the occurrence of large proportions of authigenic kaolinite along with variable contents of illite and smectite, accessory Al hydroxides and Fe and Ti oxides. They also contain detrital quartz, feldspars and mica. The composition of smectites, Al-rich and classified as montmorillonites-beidellites (Fig. 8), is characteristic of paleosols in which the parent rock consists of aluminosilicates (Chamley, 1989).

The intense dissolution of detrital silicate minerals originally present in the parent material (mainly feldspars but also from quartz, Figs. 5A, D, 6B), followed by the lixiviation of alkaline and alkaline earth elements lead to the crystallization of new phases rich in relatively immobile cations (Al, Si, Fe, Ti). The consequence of this dissolution-crystallization process was the authigenesis of kaolinite (Figs. 5A, D, 7A, D), smectite (Figs. 5B, 6B, 7B), Fe and/or Ti oxides (Fig. 7G), and Al hydroxides (Fig. 4D). The lack of intermediate phases between feldspars or quartz and kaolinite at the SEM scale is consistent with the development of dissolution-crystallization processes at the micron scale, and indicates high fluid/rock ratio during the alteration process. Furthermore in intermediate levels of the section (samples MGT-10 and MGT-14), the chemical composition of the dioctahedral clays suggest the presence of fine mixtures of smectite and illite, and upsection (samples MGT-22 and MGT-24) the smectite is progressively purer, probably because the more intense weathering conditions enhanced the smectite crystallization and illite dissolution. It is not easy to establish the crystallization sequence of the authigenic phases, though in some cases smectite seems to postdate kaolinite crystallization (Fig. 7E), but this sequence may have been different in other textural sites.

The similarity of the kaolinite textures (crystal size and morphology) in paleosols developed in different lithologies (Figs. 6B, 7D) suggests that they were not affected by recrystallization associated with diagenesis. This is consistent with previous studies that indicated that this unit

only experienced eogenetic diagenesis, as burial of the formation was of relatively short duration (Do Campo et al., 2007).

Kaolinite formation under near-surface/meteoric conditions at a regional scale is correlated to humid-subtropical to tropical climates (Chamley, 1989; Hallam et al 1991; Righi and Meunier, 1995; Ruffell et al., 2002), whereas smectite authigenesis in soil profiles requires alternating humid and dry seasons in which chemical weathering is reasonably mild or slow. On the other hand, illite-mica prevails under dry climates typically related with low hydrolyzing conditions in weathering profiles (Chamley, 1989). The contrasting humidity and temperature conditions required for the formation of both minerals led Chamley (1989) to propose Kln/Ms as a paleoclimatic indicator. However, there are other variables, apart from climate, affecting the authigenesis of clay minerals in continental sediments; mainly, source-area lithology, continental morphology and depositional environments (Chamley, 1989).

In the case of the Maíz Gordo Basin regional studies have shown that it developed during a period of relative tectonic calm associated with a low subsidence rate (Salfity and Marquillas, 1994). Moreover, the source areas of the basin, located south and southwest, were dominated by crystalline rocks and no change was detected in this provenance (Do Campo et al., 2007). Therefore the vertical changes in clay minerals relative abundances observed in the three sections, essentially the general increase in kaolinite content from bottom to the top, indicates an increase in chemical weathering with time. This is in agreement with the variation in paleosols types through time (Fig. 2). However, at Tin Tin the Maíz Gordo Fm displays significant fluctuations in kaolinite abundance and Kln/Ms superimposed on the general trend of increase of kaolinite content with time (Fig. 2C). These fluctuations in clay minerals abundances are disconnected from any lithologic or sedimentary facies control, thus the five cycles that were distinguished on the basis of Kln/Ms imply changes in the intensity of weathering, probably initiated by paleoclimate change.

The Paleocene-Eocene transition is well known to have been a warming trend (Mudelsee et al., 2014) punctuated by several periods characterized by extremely warm global temperatures or hyperthermals (Zachos et al., 2008): 1) the short Paleocene-Eocene thermal maximum (PETM, or ETM1), 2) the Early Eocene Thermal Maximum (ETM2); and 3) the Early Eocene Climatic Optimum (EECO) (Zachos et al., 2008). Maíz Gordo Fm paleosols displaying high kaolinite contents were certainly developed by intense leaching under hot-wet climatic conditions. In this context, the cyclic changes in kaolinite abundance and Kln/Ms observed in the Tin Tin section probably indicate changes in paleotemperature and mean annual precipitation (MAP) having taken place during the deposition of the Maíz Gordo Fm. Even though the duration of the weathering period can also affect Kln/Ms of paleosols, this interpretation is in agreement with the increase of ~ 5 °C at the height of the PETM as well as the high values of MAP (~1100 to ~ 1370 mm/yr) calculated for Andrews et al. (2017) on the basis of weathering indices for the upper ~30 m of the studied sections. On this it is worth mentioning that drastic changes in sedimentary facies triggered by fluctuations in water level were observed in deposits of the Maíz Gordo Fm corresponding to inner lake and lake littoral environments (del Papa, 1999). These changes in sedimentary facies were also correlated with variations in the fluvial patterns, that allowed differentiation of four main evolutionary stages in the Maíz Gordo Basin corresponding to successive periods of wetness/dryness (del Papa, 1999; Do Campo, et al., 2007). Furthermore, the changes in the sequence of precipitation between kaolinite and smectite observed at micron scale, may also suggest wetter/dryer cycles.

Moreover, kaolinite-rich paleosols of cycles III to V at Tin Tin coincide with the ~30m thick section displaying elevated Chemical Weathering Indices and negative carbon isotope excursions (CIE) reported by Andrews et al. (2017). The three negative excursions (CIE) of ~−3‰, ~−5‰ and ~−6‰ recognized by these authors correspond to the kaolinite-rich paleosol levels of each cycle as can be seen in Fig. 9. The largest CIE (−6‰) registered at the top of the Maíz Gordo Fm was

correlated by these authors with the PETM, thus the kaolinite-rich paleosols occurring at the top of the unit developed during short episodes (~ 100 to 400 kyr) of warming and increased humidity during Paleocene-early Eocene times. Therefore, we interpret the levels of high Kln/Ms as warming-wet periods and horizons rich in illite-mica as the return to relatively cooler and drier conditions. High frequency climatic fluctuation like these have been described for the continental Bighorn Basin, Wyoming in a study based on the analysis of paleosols spanning the PETM (Krauss and Riggins, 2007). In the Polecat Bench stratigraphic section these authors identified four drying episodes (D1-D4) within the main body of the CIE, and one in the pre-CIE interval. It is also worth noting that Krauss and Riggins (2007) suggest that the D1-D4 drying episodes recognized in terrestrial sediments of the Bighorn Basin may correspond to the precessional cycles identified in marine records (e.g., Norris and Röhl, 1999; Farley and Eltgroth, 2003). However, correlation of the kaolinite-rich beds of the Maíz Gordo Fm with Paleocene-Eocene hyperthermals is not completely reliable because its age is not constrained radiometrically, ven though different lines of evidence assigned this unit to the Thanetian-Lower Ypresian, which implies that it spans the Paleocene-Eocene transition (Quattrocchio et al., 2005; Hyland et al., 2015; Andrews et al., 2017).

Similar cycles of varying kaolinite abundance and Kln/Ms values were also observed at Tonco and Obelisco. In both sections kaolinite is absent at the bottom of the Maíz Gordo Fm and increases progressively up to Kln/Ms of 2.3 at Obelisco and 2.8 at Tonco (Table 2). Moreover, at Tonco another Kln/Ms peak value of 3.6 is recorded at the top of the unit. These changes in clay mineral assemblages are interpreted as further evidence of variations in paleoprecipitation and paleotemperature. However, it is not possible to perform correlations between the clay mineralogy and hyperthermal periods, because the sampling was not as detailed as at Tin Tin.

At Obelisco several levels from the Maíz Gordo Fm contain analcime, in one case in association with halite. This occurrence of analcime does not seem to have a paleoclimatic

implication, because it takes place in kaolinite-rich paleosol levels, some of them also containing purple hematite nodules. Consequently, analcime likely is of diagenetic origin in these sediments.

The basal horizons of the Lumbrera Fm are with a few exceptions dominated by illite-mica with subordinate kaolinite and smectite indicating limited ionic leaching (Chamley, 1989). Changes in clay minerals assemblages suggest a marked variation in paleoweathering conditions between the Maíz Gordo Fm and Lumbrera Fm. Such changes may be the result of a more moderate temperate-humid climate, as is also indicated by the occurrence of paleosols that were classified as calcic vertisols (Fig. 2).On the other hand, at Tin Tin the Mealla, Maíz Gordo and Lumbrera formations contain several smectite-rich levels that strongly contrast with the clay-minerals assemblage depicted by the horizons located below and above each formation. Thin tuff levels have been identified in the three units of the Santa Bárbara Subgroup (Salfity and Marquillas, 1999; Marquillas et al., 2005; Do Campo et al., 2007). Thus the sharp increase in smectite relative abundances in our study sections probably reflects a significant volcaniclastic contribution.

Our study of Paleogene terrestrial deposits, mostly consisting of paleosols, shows that paleoclimate reconstruction based on clay mineralogy correlates quite well with previously published carbon isotope data for the same stratigraphic sections (Andrews, et al., 2017) as is shown in Fig. 9. This is not unforeseen, because soils form in direct contact with the atmosphere, and are affected by climate conditions prevailing during pedogenesis, thus proxies based on paleosols are potentially a much more direct means of making paleoclimate reconstructions than those based on marine records (Sheldon and Tabor, 2009). We emphasize the importance of combining the identification of clay minerals by XRD with textural and morphological studies by electron microscopy in order to infer the origin of the clays.

Despite the lack of absolute age constrains for the Maíz Gordo Fm we have identified the Paleocene-Eocene global warming trend in the Salta Basin, located at mid paleolatitudes, and

several humid periods that promoted intense weathering and kaolinite authigenesis. Therefore, this study demonstrates that clay mineralogy is a robust paleoclimate proxy in terrestrial sediments not affected by diagenetic changes. This proxy is a good option in sequences lacking appropriate lithologies to perform isotope geochemistry.

**10. CONCLUSIONS**

Cyclic changes in kaolinite abundance and Kln/Ms were identified in Paleogene terrestrial deposits corresponding to the Maíz Gordo Fm, mostly consisting of paleosols. The morphology and texture of the clays suggest that kaolinite and smectite are authigenic and that they crystallized during pedogenesis from dissolution of silicates (mainly feldspars but also from quartz). Variations in Kln/Ms were correlated with changes in paleotemperature and mean annual precipitation having taken place during the deposition of the Maíz Gordo Fm with higher Kln/Ms values corresponding to warming-wet periods that triggered intense chemical weathering. Taking into account that a previous study of the paleosols in the upper 30 m of the studied sections records three negative CIE in organic matter carbon, and correlated one of them with the Paleocene to early Eocene Thermal Maximum (Andrews et al., 2017), the cyclic changes in kaolinite relative abundances identified in the Maíz Gordo Fm constitute strong evidence for the occurrence of several short-lived (~ 100 to 400 kyr) hyperthermals during Paleocene-early Eocene times in the Southern Hemisphere that likely coincided with well-established warming episodes for the Northern Hemisphere. Different studies of marine and terrestrial records have concluded that this short-term variability in climate was modulated by orbital forcing, specifically precession and eccentricity (Krauss and Riggins, 2007; Zachos et al., 2010).

The basal levels of the Lumbrera Fm are, with a few exceptions, dominated by illite-mica with subordinate kaolinite and smectite, indicating limited ionic leaching (Chamley, 1989). Changes in clay minerals assemblages suggest marked variation in paleoweathering conditions between the Maíz Gordo and Lumbrera formations. The contrasting paleosol types, gleyed oxisols

and calcic vertisol prevailing, respectively, at the top of the Maíz Gordo Fm and the base of the Lumbrera Fm, indicate that such changes were paleoclimate driven. This study demonstrates that clay mineralogy is a robust paleoclimate proxy in terrestrial sediments not affected by diagenetic changes.

**ACKNOWLEDGMENTS**

The help of Cristina Gallego with FESEM (University of Zaragoza) was essential for the present work. The authors would like to acknowledge the use of the Servicio General de Apoyo a la Investigación-SAI, University of Zaragoza. A. Baleirón prepared the samples for X ray diffraction, and G. Giordanengo helped with the digital figures. This work was partially financed by Research Projects CGL2011-30153-C02-01, CGL2013-46169-C2-1-P (Spanish Ministry of Science), and the Gobierno de Aragón and the European Social Fund (Grupos Consolidados) and also ANCyT - PICT-2011-0407 grant (Argentina). C. de Papa thanks PUE-CICTERRA 2016. The authors also like to thank the Ministerio de Ambiente y Desarrollo Sustentable, Salta Province, the Programa Areas Protegidas, Secretaria de Ambiente, Salta Government and the guards of the Reserva Manejada Quebrada de las Conchas for permission to work in the Quebrada de las Conchas Park, and also to the Salta branch of Parques Nacionales and Parque Nacional Los Cardones. We deeply thank the revision and handling by the editor Prof. Jasper Knight, and the suggestions by an anonymous reviewer, which significantly improved a previous version of the manuscript.

Appendix A. Supplementary data

Structural formulae of dioctahedral smectite calculated on the basis of 22 negative charges ($O_{10}(OH)_2$), based on EDS microanalyses can be found online as supplementary data.

**REFERENCES**

Andrews, E., White, T., del Papa C., 2017. Paleosol-based paleoclimate reconstruction of the Paleocene-Eocene Thermal Maximum, northern Argentina. Palaeogeography, Palaeoclimatology, Palaeoecology 471, 181-195.

Baczynski, A.A., McInerney, F.A., Scott, L.W., Kraus, M.J., Bloch, J.I., Secord, R., 2017. Constraining paleohydrologic change during the Paleocene-Eocene Thermal Maximum in the continental interior of North America. Palaeogeography, Palaeoclimatology, Palaeoecology 465, 237-246.

Bauluz, B., Yuste, A., Mayayo, M.J., Canudo, J.I., 2014. Early kaolinization of detrital Weald facies in the Galve Sub-basin (Central Iberian Chain, north-east Spain) and its relationship to palaeoclimate. Cretaceous Research 50, 214-227.

Bridge, J.S., 2003. Rivers and Floodplains, Forms, Processes, and Sedimentary Record. Blackwell Publishing, Oxford, 491 pp.

Bullock, P., Fedoroff, N., Jongerius, A., Stoops, G., Tursina, T., 1985. Handbook for soil thin section description. Waine Research, Wolverhampton, 152 pp.

Buurman, E., Meijer, E.L., van Wijck J.H., 1988. Weathering of chlorite and vermiculite in ultramafic rocks of Cabo Ortegal, northwestern Spain. Clays and Clay Minerals 36, 263-269.

Chamley, H., 1989. Clay Sedimentology. Springer Verlag, Berlin, 623 pp.

Charles, A.J., Condon, D.J., Harding, I.C., Pälike, H., Marshall, J.E.A., Cui, Y., Kump, L., Croudace, I.W., 2011. Constraints on the numerical age of the Paleocene Eocene boundary. Geochemistry, Geophysics, Geosystems 12, Q0AA17, doi:10.1029/2010GC003426.

Clechenko, E., Kelly, D., Harrington, G., Stiles, C., 2007. Terrestrial records of a regional weathering profile at the Paleocene-Eocene boundary in the Williston Basin of North Dakota. Geological Society of America Bulletin 119, 428–442.

del Papa, C.E., 1999. Sedimentation on a ramp type lake margin: Paleocene-Eocene Maíz Gordo Formation, northwestern Argentina. Journal of South American Earth Sciences 12, 389-400.

del Papa C.E., Salfity, J.A., 1999. Non-marine Paleogene sequences, Salta Group, Northwest Argentina. Acta Geológica Hispánica 34, 105–122.

del Papa, C., Kirschbaum, A.,., Powell, J., Brod, A., Hongn, F., Pimentel, M., 2010. Sedimentological, geochemical and paleontological insights applied to continental omission surfaces: a new approach for reconstructing Eocene foreland basin in NW Argentina. Journal of South American Earth Sciences 29, 327-345.

Do Campo, M., del Papa, C., Jiménez-Millán, J., Nieto, F., 2007. Clay mineral assemblages and analcime formation in a Palaeogene fluvial–lacustrine sequence (Maíz Gordo Formation Palaeogen) from northwestern Argentina. Sedimentary Geology 201, 56-74.

Domingo, L., López Martinez, N., Leng, M.J., Grimes, S.T., 2009. The Paleocene Eocene Thermal Maximum record in the organic matter of the Claret and Tendruy continental sections (South central Pyrenees, Lleida, Spain). Earth and Planetary Science Letters 281, 226–237.

Farley, K.A., Eltgroth, S.F., 2003. An alternative age model for the Paleocene–Eocene thermal maximum using extraterrestrial $^{3}$He. Earth and Planetary Science Letters 208, 135–148.

Genise, J., Cantil, L., Bellosi, E., 2016, Lower Paleogene complex ant nests from Argentina: evidence for early polydomy in ants? Palaios 31, 549-562.

Güven, N., 1988. Smectites. In: Bailey S.W., Hydrous Pyllosilicates. Mineralogical Society of America, Reviews in Mineralogy 19, pp 497-559.

Hajek, E.A., Wolinsky, M.A., 2012. Simplified process modeling of river avulsion and alluvial architecture: Connecting models and field data. Sedimentary Geology 257-260, 1-30.

Hallan, A., Grose, J.A., Ruffell, A.H., 1991. Paleoclimatic significance of changes in clay mineralogy across the Jurassic Cretaceous boundary in England and France. Palaeogeography, Palaeoclimatology, Palaeoecology 81, 173-187.

Hyland, E.G., Sheldon, N.D., Cotton, J.M., 2015. Terrestrial evidence for a two-stage mid-Paleocene biotic event. Palaeogeography, Palaeoclimatology, Palaeoecology 417, 371–378.

Hyland, E.G., Sheldon, N.D., Cotton, J.M., 2017. Constraining the early Eocene climatic optimum: A terrestrial interhemispheric comparison. Geological Society of America Bulletin 129, 244–252.

Kennett, J.P., Stott, L.D., 1991. Abrupt deep-sea warming, palaeoceanographic changes and benthic extinctions at the end of the Palaeocene. Nature 353, 225–229.

Koch, P., Clyde, W., Hepple, R., Fogel, M., Wing, S., Zachos, J., 2003. Carbon and Oxygen Isotope Records from Paleosols Spanning the Paleocene-Eocene Boundary, Bighorn Basin, Wyoming. In: Wing, S., Gingerich, P., Schmitz, B., Thomas, E. (Eds.), Causes and Consequences of Globally Warm Climates in the Earl Paleogene. Geological Society of America Special Paper 369, pp. 49–64.

Koch, P.L., Zachos, J.C., Dettman, D.L., 1995. Stable isotope stratigraphy and paleoclimatology of the Paleogene Bighorn Basin (Wyoming, USA). Palaeogeography, Palaeoclimatology, Palaeoecology 115, 61–89.

Koch, P.L., Zachos, J.C., Gingerich, P.D., 1992. Correlation between isotope records in marine and continental carbon reservoirs near the Palaeocene/Eocene boundary. Nature 358, 319-322.

Kraus, M.J., Riggins, S., 2007. Transient drying during the Paleocene-Eocene Thermal Maximum (PETM): analysis of paleosols in the Bighorn Basin, Wyoming. Palaeogeography, Palaeoclimatology, Palaeoecology 245, 444-461.

Mack, G.H., Calvin, J.W., 1992. Paleosols for Sedimentologists. Geological Society of America Short Course Notes, Presented on the Occasion of the Annual Meeting of the Geological Society of America, October 26–29, 1992, Cincinnati, Ohio, 127 pp.

Mack, G.H., Calvin, J.W., Monger, C.H., 1993. Classification of paleosols. Geological Society of America Bulletin 105, 129–136.

Marquillas, R.A, del Papa, C.E., Sabino, I., 2005, Sedimentary aspects and paleoenvironmental evolution of a rift basin: Salta Group (Cretaceous-Paleogene), northwestern Argentina: International Journal of Earth Sciences 94, 94-113.

Matheos, S., del Papa, C., 2003. Oolitic facies in carbonate lacustrine deposits of Maíz Gordo formation (Palaeogene) in the northwest argentine. III Congreso Latinoamericano de Sedimentología, Belem, Brasil, Actas, 2, 41.

Martin, J.D., 2004. Using XPowder: A software package for powder X-ray diffraction analysis, 105 pp. (Retrieved 18 April 2007 from www.xpowder.com).

McInerney, F.A., Wing, S.L., 2011. The Paleocene-Eocene Thermal Maximum: a perturbation of carbon cycle, climate, and biosphere with implications for the future. Annual Review of Earth and Planetary Sciences 39, 489–516.

Moore, D.M., Reynolds, R.C., 1997. X-Ray diffraction and the identification and analysis of clay minerals. Oxford University Press, New York, 378 pp.

Mudelsee, M., Bickert, T., Lear, C.H., Lohmann, G., 2014. Cenozoic climate changes: A review based on time series analysis of marine benthic $\delta^{18}O$ records. Reviews of Geophysics 52, 333–374.

Murakami, T., Isobe, H., Sato, T., Ohnuki, T., 1996. Weathering of chlorite in a quartz-chlorite schist. Mineralogical and chemical changes. Clays and Clay Minerals 44, 244-256.

Nanson, G.C., Croke, J.C.A., 1992. Genetic classification of floodplains. Geomorphology 4, 459-486.

Nichols, G., 2009. Sedimentology and Stratigraphy, Second Edition. Wiley-Blackwell, Oxford, 411 pp.

Norris, R.D., Röhl, U., 1999. Carbon cycling and chronology of climate warming during the Paleocene/Eocene boundary. Nature 401, 775–778.

Quattrocchio, M.E., Volkheimer, W., Marquillas, R.A., Salfity, J.A., 2005. Palynostratigraphy, palaeobiogeography and evolutionary significance of the late Senonian and early Paleogene

palynofloras of the Salta group, northern Argentina. Revista Española de Micropaleontología 37, 259–272.

Raucskik, B., Varga, A., 2008. Climato-environmental controls on clay minerals of the Hettangian-Bajocian succession of the Mecsek Mountains (Hungary): An evidence for extreme continental weathering during the early Toarcian oceanic anoxic event. Palaeogeography, Palaeoclimatology, Palaeoecology 265, 1-13.

Righi, D., Meunier, A., 1995. Origin of clays by rock weathering and soil formation. In: Velde, B., Origin and mineralogy of clays: clays and the environment. Springer-Verlag, Heidelberg, pp. 43-161.

Robert, C., Kennett, J., 1994. Antarctic subtropical humid episode at the Paleocene-Eocene boundary: clay mineral evidence. Geology 22, 211–214.

Röhl, U., Westerhold, T., Bralower, T.J., Zachos, J.C., 2007. On the duration of the Paleocene Eocene Thermal Maximum (PETM). Geochemistry, Geophysics, Geosystems 8, Q12002, doi:10.1029/2007GC001784.

Ruffell, A., McKinley, J.M., Worden, R.H., 2002. Europe Comparison of clay mineral stratigraphy to other proxy palaeoclimate indicators in the Mesozoic of NW Europe. Philosophical Transactions of the Royal Society of London A 360, 675-693.

Rust, B.R., 1972. Structure and process in a braided river. Sedimentology 18, 221-245.

Salfity, J.A., Marquillas, R.A., 1994. Tectonic and sedimentary evolution of the Cretaceous-Eocene Salta Group Basin, Argentina. In: Salfity, J.A.,) Cretaceous Tectonics of the Andes. Springer, Braunschweig, 348 pp.

Salfity, J.A., Marquillas, R.A., 1999. La cuenca Cretácico-Terciaria del Norte Argentino. In: Caminos R., Geología Argentina. Subsecretaría de Minería de la Nación, SEGEMAR, An 29, Buenos Aires, pp. 613-626.

Schmitz, B., Pujalte, V., 2007. Abrupt increase in seasonal extreme precipitation at the Paleocene Eocene boundary. Geology 35, 215–218.

Sheldon, N.D., Tabor, N.J., 2009. Quantitative paleoenvironmental and paleoclimatic reconstruction using paleosols. Earth-Science Reviews 95, 1–52.

Sluijs, A., Bowen, G.J., Brinkhuis, H., Lourens, L.J., Thomas, E., 2007. The Palaeocene-Eocene Thermal Maximum super greenhouse: biotic and geochemical signatures, age models and mechanisms of global change. In: Williams, M., Haywood, A.M., Gregory, F.J., Schmidt, D.N. (Eds.), Deep-Time Perspectives on Climate Change: Marrying the Signal from Computer Models and Biological Proxies. The Micropalaeontological Society, Special Publications. The Geological Society, London, pp. 323–349.

Sluijs, A., Schouten, S., Pagani, M., Woltering, M., Brinkhuis, H., Damtsé, J.S.S., Dickens, G.R., Huber, M., Reichart, G.J., Stein, R., Matthiessen, J., Lourens, L.J., Pedentchouk, N., Backman, J., Moran, K., the Expedition 302 Scientists, 2006. Subtropical Arctic Ocean temperatures during the Palaeocene/Eocene thermal maximum. Nature 441, 610–613.

Tripati, A., Elderfield, H., 2005. Deep-sea temperature and circulation changes at the Paleocene-Eocene Thermal Maximum. Science 308, 1894–1898.

Vergani, G., Starck, D., 1989. Aspectos estructurales del Valle de Lerma al sur de la Ciudad de Salta. Boletín de Información Petrolera 16, 2-9.

Viramonte, J.G., Kay, S.M., Becchio, R., Escayola, M., Novitski, I., 1999. Cretaceous rift related magmatism in central-western South America. Journal of South American Earth Sciences 12, 109–121.

Weaver, C.E., 1989. Clays, Muds, and Shales. Developments in Sedimentology, 44. Elsevier, Amsterdam, 818 pp.

Westerhold, T., Röhl, U., Raffi, I., Fornaciari, E., Monechi, S., Reale, V., Bowles, J., Evans, H.F., 2008. Astronomical calibration of the Paleocene time. Palaeogeography, Palaeoclimatology, Palaeoecology 257, 377–403.

White, T., del Papa, C. Andrews, E., 2017. Chronostratigraphy of Paleogene strata, Salta Basin, northwestern Argentina: A reply to Hyland and Sheldon's comment. Palaeogeography, Palaeoclimatology, Palaeoecology (in press).

White, P.D., Schiebout, J., 2008. Paleogene paleosols and changes in pedogenesis during the initial Eocene Thermal Maximum: Big Bend National Park, Texas, USA. Geological Society of America Bulletin 12, 1347–1361

Zachos, J.C., Gerald, R., Dickens, G.R., Zeebeet, R.E., 2008. An early Cenozoic perspective on greenhouse warming and carbon-cycle dynamics. Nature 451, 279-283.

Zachos, J. C., McCarren, H., Murphy, B., Röhl, U., Westerhold, T., 2010. Tempo and scale of late Paleocene and early Eocene carbon isotope cycles: Implications for the origin of hyperthermals. Earth and Planetary Science Letters 299, 242–249.

Zachos, J.C., Lohmann, K.C., Walker, J.C.G., Wise, S.W., 1993. Abrupt climate change and transient climates during the Paleogene: a marine perspective. The Journal of Geology 101, 191–213.

Zachos, J., Pagani, M., Sloam, L., Thomas, E., Billups, K., 2001. Trends, rhythms, aberrations in global climate 65 Ma to present. Science 292, 686–693.

Zachos, J.C., Röhl, U, Schellenberg, S.A., Sluijs, A., Hodell, D.A., Kelly, D.C., Thomas, E., Nicolo, M., Raffi, I., Lourens, L.J., McCarren, H., Kroon, D., 2005. Rapid acidification of the ocean during the Paleocene-Eocene Thermal Maximum. Science 308, 1611–1615.

Zachos, J.C., Wara, M.W., Bohaty, S., Delaney, M.L., Petrizzo, M.R., Brill, A., Bralower, T.J., Premoli-Silva, I., 2003. A transient rise in tropical sea surface temperature during the Paleocene-Eocene thermal maximum. Science 302, 1551–1554.

Zeebe, R., Ridgwell, A., Zachos, J., 2016. Anthropogenic carbon release rate unprecedented during the past 66 million years. Nature Geoscience 9, 325–329.

**Figure and Table captions**

Table 1. Mineralogical composition of the clay fraction in the Tin Tin section based on XRD results. Semi-quantitative abundances of clay minerals (%) and Kln/Ms ratios were calculated employing MIF factors proposed by Moore and Reynolds (1997). Samples in bold were studied by SEM.

Table 2. Mineralogical composition of the clay fraction in the Tonco and Obelisco sites based on XRD results. Semi-quantitative abundances of clay minerals (%) and Kln/Ms ratios were calculated employing MIF factors proposed by Moore and Reynolds (1997). Samples in bold were studied by SEM.

Figure 1. (A) Satellite image of northwestern Argentina. Sampling sites and areas shown in geological maps are indicated (Tin Tin, Tonco and Obelisco). (B) Geological map of the Tin Tin and Tonco areas. (C) Geological map of the Obelisco area. Geologic maps B and C modified from Vergani and Starck (1989).

Figure 2. (A) Stratigraphic log of the Palaeogene Tin Tin sequences. The box indicates the section studied by Andrews et al. (2017) this area is enlarged in Fig. 9. (B) Paleosol types along the stratigraphic column. (C) Variation of kaolinite, illite, smectite and I/S relative abundances (%) along the stratigraphic log, and cycles identified according to Kln/Ms. Dotted arrow indicates the general trend of increase in kaolinite abundance from the bottom to the top of the Maíz Gordo Fm.

Figure 3. Field photographs of the studied deposits at Tin Tin. (A) Conglomeratic channel-fill (CH) facies association. (B) Fine-grained floodplain (OF) facies association. (C) Calcic vertisol paleosol level from the lower section of the Maíz Gordo Formation. (D) Inseptisol paleosol typical of the upper section of the Maíz Gordo Formation.

Figure 4. SE images showing themorphology of clays. (A) Smectite flakes. (B) Euhedral to subhedral kaolinite plates. (C) Anhedral illite plates. (D) Acicular aluminium hydroxides. Abbreviations of minerals according to Kretz (1983) and updated by Whitney and Evans (2010). Sm: smectite, Kln: kaolinite, Ilt: illite, $Al(OH)_3$: aluminium hydroxide.

Figure 5. BSE images. Texture of samples from cycles I and II. (A) Silty claystone exhibiting a heterometric and heterogeneous texture with abundant detrital fragments of quartz and K feldspar, and a matrix composed of abundant clays (MGT-10). (B) Claystone (MGT-14) depicting a heterometric and heterogeneous texture and a matrix mainly composed of smectite, a detrital mica/kaolinite intergrowths (upper left). (C) Smectite packets forming the matrix of a claystone exhibiting a curved lens-shaped morphology with no preferred orientation, and kaolinite showing its typical platy morphology indicating an authigenic origin (MGT-14). (D) Kaolinite and smectite having replaced K feldspar and albite fragments in claystone MGT-10. Qtz: quartz, Kf: potassium feldspar, Sm: smectite, Kln: kaolinite, Ilt: Illite, Ms/Kln: mica-kaolinite intergrowhts.

Figure 6. BSE images of a kaolinite-rich claystone from cycle III (MGT 22). (A) Claystone displaying a heterometric and heterogeneous texture with abundant detrital fragments of quartz and K feldspar. (B) Detail of the matrix composed by booklets of kaolinite showing the typical platy morphology and smectite packets exhibit the characteristic curved lens-shaped morphology, with no preferred orientation, an albite fragment intensively altered and replaced by smectite (upper left. (C) Detrital subangular fragments of quartz and feldspar and smectite packet depicting a curved lens-shaped morphology in the matrix. Qtz: quartz, Kf: K-feldspar, Sm: smectite, Kln: kaolinite, Ab: albite.

Figure 7. BSE images of a kaolinite-rich siltstone from cycle III (MGT-24). (A) Detrital fragment of K-feldspar replaced by kaolinite and smectite and packets of smectite depicting a curved lens-shaped morphology in the matrix. (B) Detail of the packets of smectite that have replaced a detrital K-feldspar fragment. (C) Detail of the smectite packets composing the matrix. (D) Kaolinite

replacing K-feldspar showing a platy morphology and forming well-developed booklets, indicating an authigenic origin. (E, F) Detail of the clays replacing a K-feldspar fragment; packets of smectite surround (white arrow) the kaolinite booklets suggesting that it was formed later than kaolinite. (G) Smectite plates associated with iron oxides in the matrix. Sm: smectite, Kln: kaolinite, Kf: K-feldspar, FeOx: iron oxides.

Figure 8. Compositional plots for smectite-type clays EDS-FESEM microanalyses. (A) Si – K, (B) Si – Interlayer charge, (C) Si – Al total, (D) Si – Mg, the limit between the montmorillonite and beidellite fields has been indicated.

Figure 9. (A) Detail of the stratigraphic log of the Tin Tin section depicted in Fig. 2 showing the upper levels of the Maíz Gordo Fm characterized by elevated Chemical Weathering Indices and negative CIE according to Andrews et al. (2017). Comparison of (B) variation of kaolinite, illite, smectite and I/S relative abundances (%) and (C) carbon isotope ($\delta^{13}C_{org}$) reported by Andrews et al. (2017).

Appendix A. Supplementary data. Smectite formula calculated from EDS data on the basis of 11 oxygens. I.Ch.: Interlayer Charge, $Al^{VI}$: Tetrahedral Al, $Al^{VI}$: Octahedral Al, $\Sigma$oct: Number of octahedral cations.

Table 1

| **Tin Tin Site** Unit | | % Illite-Mica | % Kln | % Sm | % I/S | Kln/Ms | |
|---|---|---|---|---|---|---|---|
| LUMRERA Fm. | LUT 30 | 80 | 9 | 11 | | 0.11 | |
| | LUT 29c | 88 | 11 | 1 | | 0.12 | |
| | LUT 29b | 81 | 10 | 9 | | 0.13 | |
| | LUT 29a | 38 | 7 | 55 | | 0.19 | |
| | LUT 28C | 80 | 12 | 8 | | 0.15 | |
| | LUT28B | 55 | 21 | 24 | | 0.37 | |
| MAÍZ GORDO Fm. | MGT 28A | 31 | 65 | 4 | | 2.10 | cycle V |
| | MGT 28 | 21 | 69 | 4 | 6.3 | 3.33 | |
| | MGT 27 | 40 | 56 | 4 | | 1.40 | cycle IV |
| | MGT 26 | 19 | 75 | 6 | | 3.91 | |
| | MGT 25 | 60 | 35 | 5 | | 0.59 | cycle III |
| | **MGT 24** | 39 | 59 | 1 | | 1.52 | |
| | MGT 23 b | 31 | 64 | 4 | | 2.04 | |
| | MGT 23 | 36 | 60 | 3 | | 1.68 | |
| | **MGT 22** | 16 | 82 | 2 | | 5.19 | |
| | MGT 21 | 25 | 68 | 7 | | 2.70 | |
| | MGT 20B | 34 | 63 | 3 | | 1.86 | |
| | MGT 20A | 44 | 54 | 2 | | 1.23 | |
| | MGT 20 | 31 | 66 | 2 | | 2.11 | |
| | MGT 19 | 64 | 32 | 4 | | 0.50 | cycle II |
| | MGT 18 | 41 | 20 | 38 | | 0.49 | |
| | MGT 17 | 48 | 42 | 9 | | 0.88 | |
| | MGT 16 | 26 | 70 | 4 | | 2.71 | |
| | MGT 15 | 23 | 62 | 15 | | 2.65 | |
| | **MGT 14** | 45 | 50 | 5 | | 1.10 | |
| | MGT 13 | 51 | 44 | 6 | | 0.86 | |
| | MGT 12 | 51 | 43 | 6 | | 0.83 | cycle I |
| | **MGT 10** | 43 | 56 | 1 | | 1.32 | |
| | MGT 9 | 45 | 45 | 10 | | 1.01 | |
| | MGT 8 | 56 | 30 | 14 | | 0.53 | |
| | **MGT 7** | 56 | 38 | 6 | | 0.68 | |
| | MGT 6 | 79 | 0 | 21 | | 0.00 | |
| MEALLA Fm. | MET 5 | 78 | 0 | 22 | | 0.00 | |
| | MET 4 | 82 | 0 | 18 | | 0.00 | |
| | MET 3 | 47 | 0 | 53 | | 0.0 | |
| | MET 2 | 5 | 11 | 84 | | 2.05 | |
| | MET 1 | 73 | 0 | 27 | | 0 | |

Table 2

A

| **Tonco Site** Unit | | % Illite-Mica | % Kln | % Sm | Kln/Ms |
|---|---|---|---|---|---|
| LUMBRERA Fm. | LULE-13 | 54 | 39 | 6 | 0.72 |
| | LULE-12 | 57 | 39 | 4 | 0.69 |
| MAÍZ GORDO Fm. | MG-LE 11 | 24 | 76 | 0 | 3.19 |
| | MG-LE 10 | 21 | 76 | 3 | 3.60 |
| | MG-LE 9 | 28 | 71 | 1 | 2.50 |
| | MG-LE 8 | 22 | 59 | 18 | 2.64 |
| | MG-LE 7 | 25 | 71 | 4 | 2.84 |
| | MG-LE 6 | 28 | 70 | 2 | 2.49 |
| | MG-LE 5 | 45 | 47 | 8 | 1.06 |
| | MG-LE4 | 48 | 49 | 4 | 1.03 |
| | MG-LE2 | 61 | 18 | 22 | 0.29 |
| | MG-LE1 | 74 | 2 | 24 | 0.03 |

B

| **Obelisco Site** Unit | | % Illite-Mica | % Kln | % Sm | Kln/Ms |
|---|---|---|---|---|---|
| LUMBRERA Fm. | LU 7 a | 80 | 14 | 6 | 0.2 |
| MAÍZ GORDO Fm. | MG 6c | 40 | 60 | - | 1.50 |
| | MG 6 b | 29 | 68 | 3 | 2.34 |
| | MG 6 a | 30 | 69 | 1 | 2.29 |
| | MG 5 c | 40 | 54 | 6 | 1.36 |
| | MG 5 b | 40 | 54 | 6 | 1.37 |
| | MG 5a | 35 | 36 | 29 | 1.03 |
| | MG 4 | 39 | 59 | 2 | 1.51 |
| | MG 3 b | 91 | - | 9 | - |
| | MG 3 a | 93 | - | 7 | - |
| MEALLA Fm. | ME-O 2 | 87 | - | 13 | - |
| | ME-O 1 c | 75 | - | 25 | - |
| | ME-O 1 b | 94 | - | 6 | - |

HIGHLIGHTS

- Development of of calcic vertisols and gleyed oxisols in Paleogene
- Connections between clay mineralogy and paleoclimatic variations during Paleogene
- Crystallization of Kaolinite and smectite in Paleocene-Eocene paleosols
- Cyclic increase in Kln/Ms indicating rises in paleoprecipitacion and paleotemperature

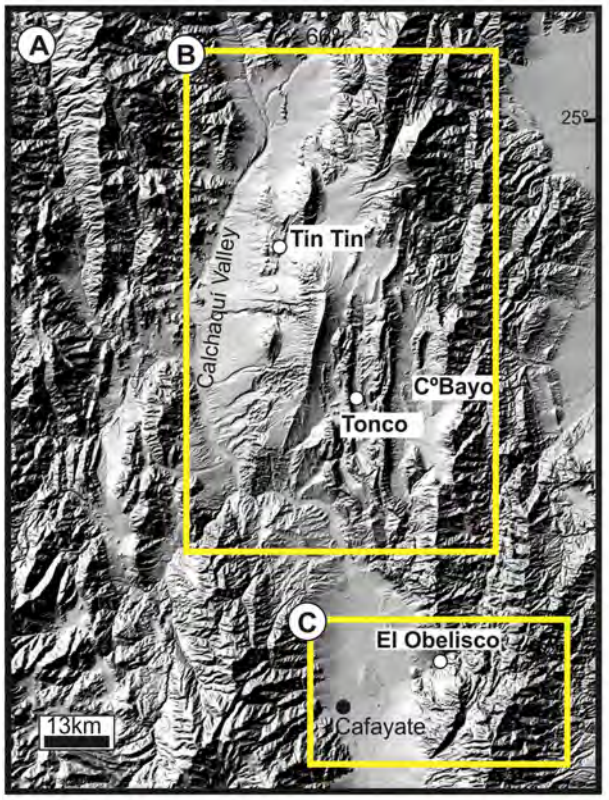
A
B
66°
25°
Calchaquí Valley
Tin Tin
CºBayo
Tonco
C
El Obelisco
Cafayate
13km

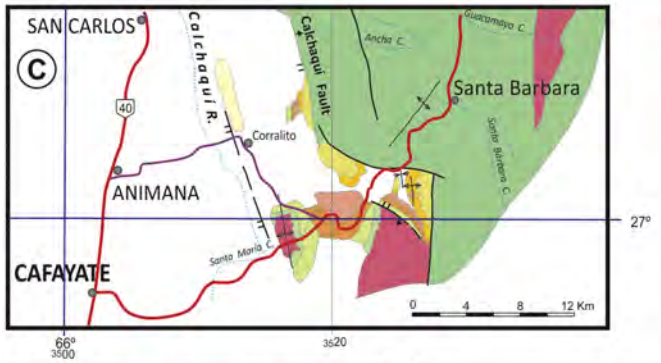
SAN CARLOS
C
Calchaquí R.
Cachaqui Fault
Ancha C.
Guacamaya C.
Santa Barbara
Santa Bárbara C.
Corralito
ANIMANA
CAFAYATE
Santa María C.
40
27°
0 4 8 12 Km
66°
3500
3520

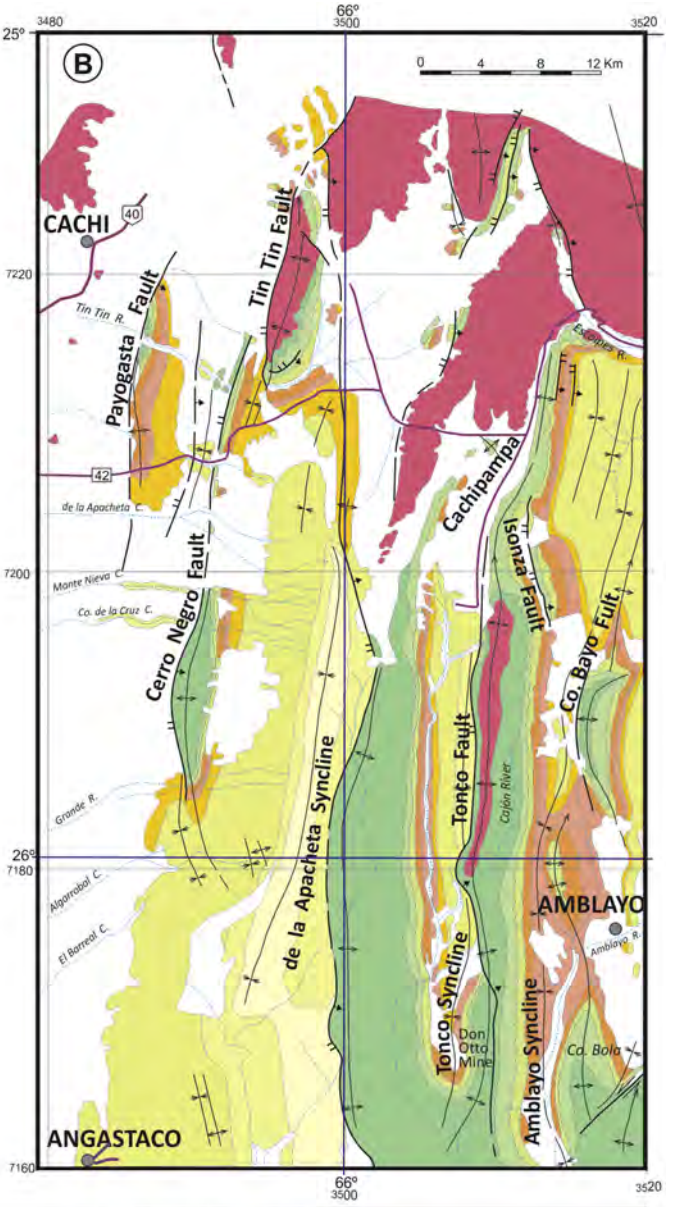
B
0 4 8 12 Km
CACHI
40
42
25°
26°
7220
7200
7180
7160
3480
3500
3520
Tin Tin Fault
Payogasta Fault
Tin Tin R.
de la Apacheta C.
Monte Nieva C.
Co. de la Cruz C.
Cerro Negro Fault
Cachipampa
Isonza Fault
Co. Bayo Fult
Grande R.
Algarrobal C.
El Barreal C.
de la Apacheta Syncline
Tonco Fault
Cajón River
AMBLAYO
Amblayo R.
Tonco Syncline
Don Otto Mine
Amblayo Syncline
Co. Bola
ANGASTACO


LOCATION MAP
REPUBLICA ARGENTINA

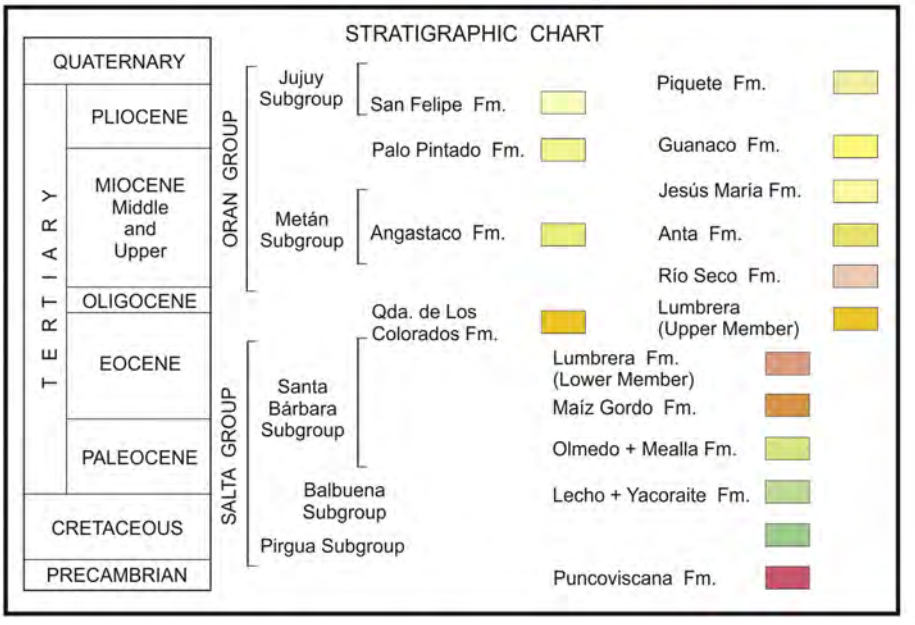
STRATIGRAPHIC CHART
QUATERNARY
TERTIARY
PLIOCENE
MIOCENE Middle and Upper
OLIGOCENE
EOCENE
PALEOCENE
CRETACEOUS
PRECAMBRIAN
ORAN GROUP
Jujuy Subgroup
San Felipe Fm.
Palo Pintado Fm.
Metán Subgroup
Angastaco Fm.
Qda. de Los Colorados Fm.
SALTA GROUP
Santa Bárbara Subgroup
Balbuena Subgroup
Pirgua Subgroup
Piquete Fm.
Guanaco Fm.
Jesús María Fm.
Anta Fm.
Río Seco Fm.
Lumbrera (Upper Member)
Lumbrera Fm. (Lower Member)
Maíz Gordo Fm.
Olmedo + Mealla Fm.
Lecho + Yacoraite Fm.
Puncoviscana Fm.

Figure 1

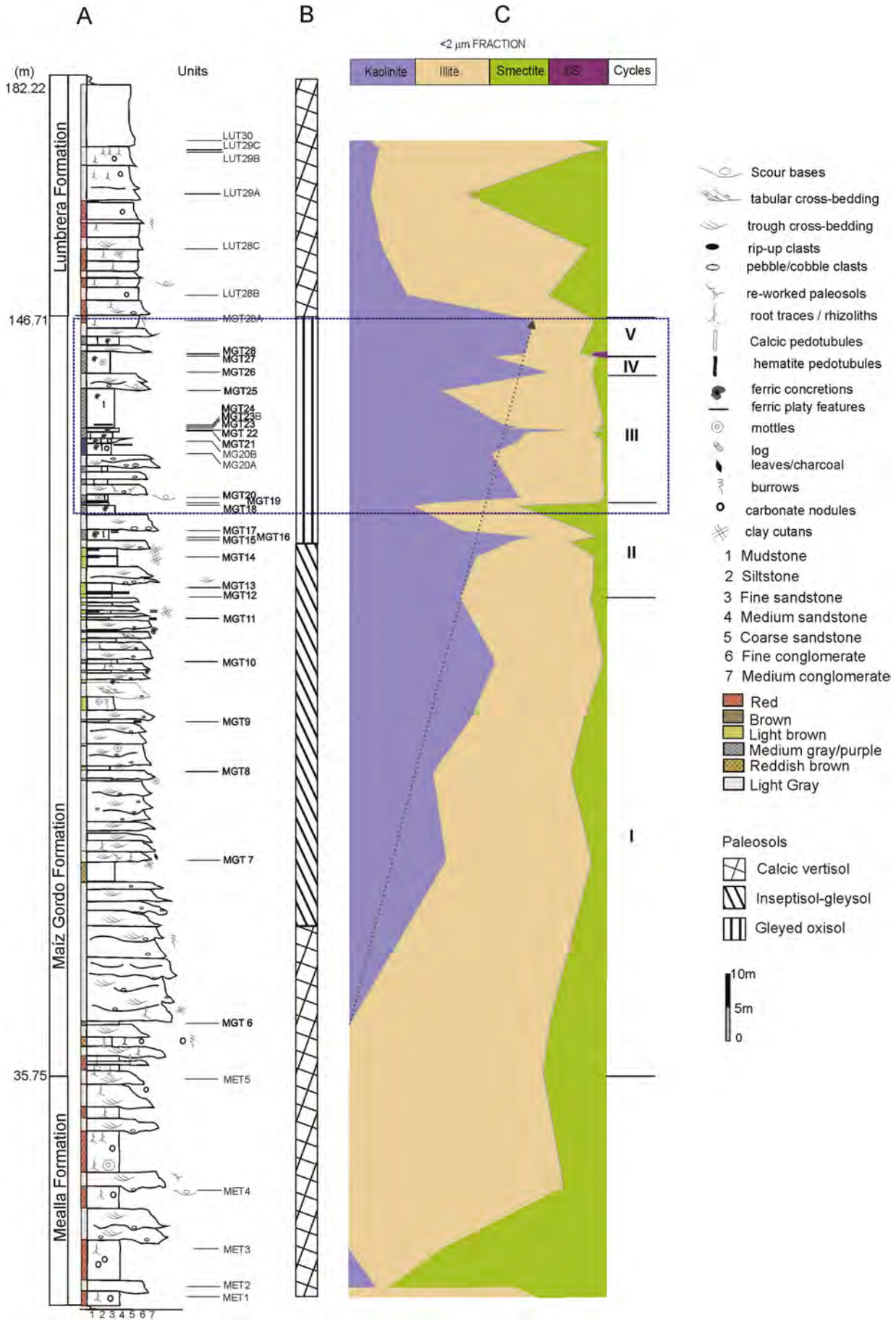
A
B
C
<2 μm FRACTION
Kaolinite
Illite
Smectite
I/S
Cycles
(m)
Units
182.22
146.71
35.75
Lumbrera Formation
Maíz Gordo Formation
Mealla Formation
LUT30
LUT29C
LUT29B
LUT29A
LUT28C
LUT28B
MGT28A
MGT28
MGT27
MGT26
MGT25
MGT24
MGT23B
MGT23
MGT 22
MGT21
MG20B
MG20A
MGT20
MGT19
MGT18
MGT17
MGT15
MGT16
MGT14
MGT13
MGT12
MGT11
MGT10
MGT9
MGT8
MGT 7
MGT 6
MET5
MET4
MET3
MET2
MET1
1 2 3 4 5 6 7
V
IV
III
II
I
Scour bases
tabular cross-bedding
trough cross-bedding
rip-up clasts
pebble/cobble clasts
re-worked paleosols
root traces / rhizoliths
Calcic pedotubules
hematite pedotubules
ferric concretions
ferric platy features
mottles
log
leaves/charcoal
burrows
carbonate nodules
clay cutans
1 Mudstone
2 Siltstone
3 Fine sandstone
4 Medium sandstone
5 Coarse sandstone
6 Fine conglomerate
7 Medium conglomerate
Red
Brown
Light brown
Medium gray/purple
Reddish brown
Light Gray
Paleosols
Calcic vertisol
Inseptisol-gleysol
Gleyed oxisol
10m
5m
0

Figure 2

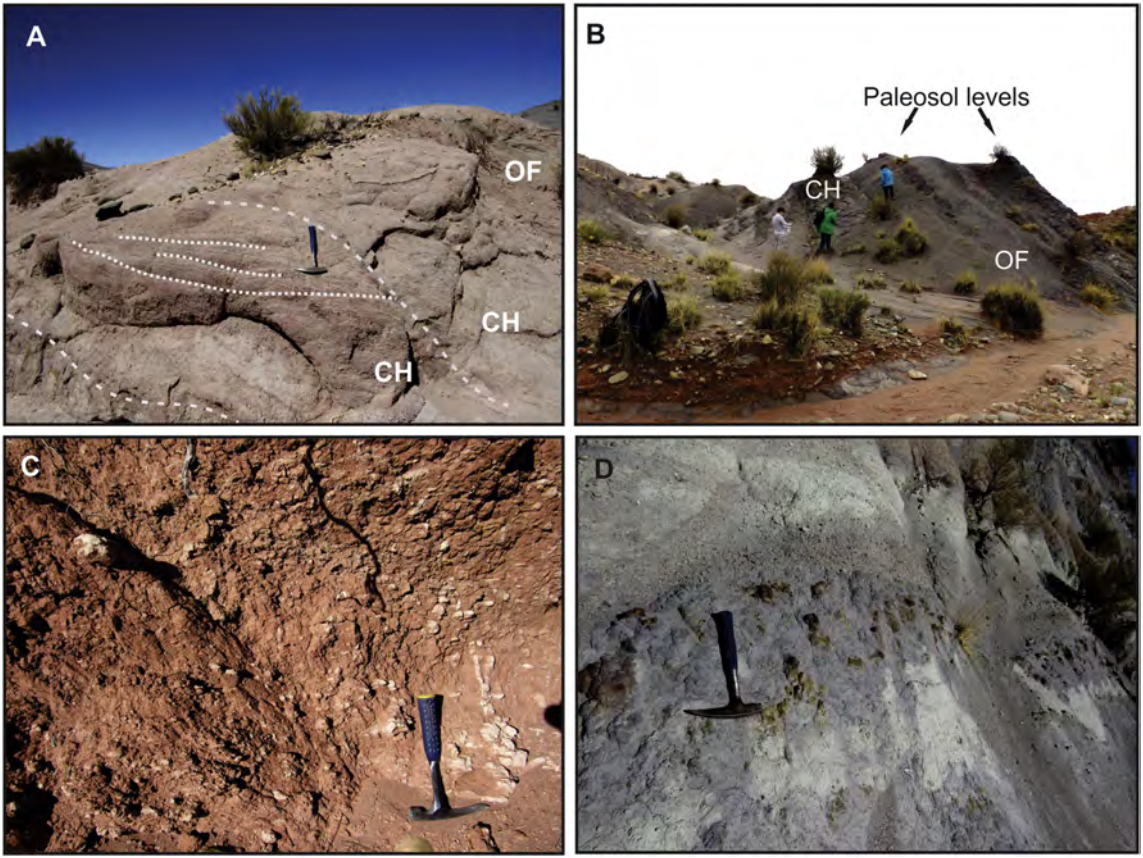


Figure 3

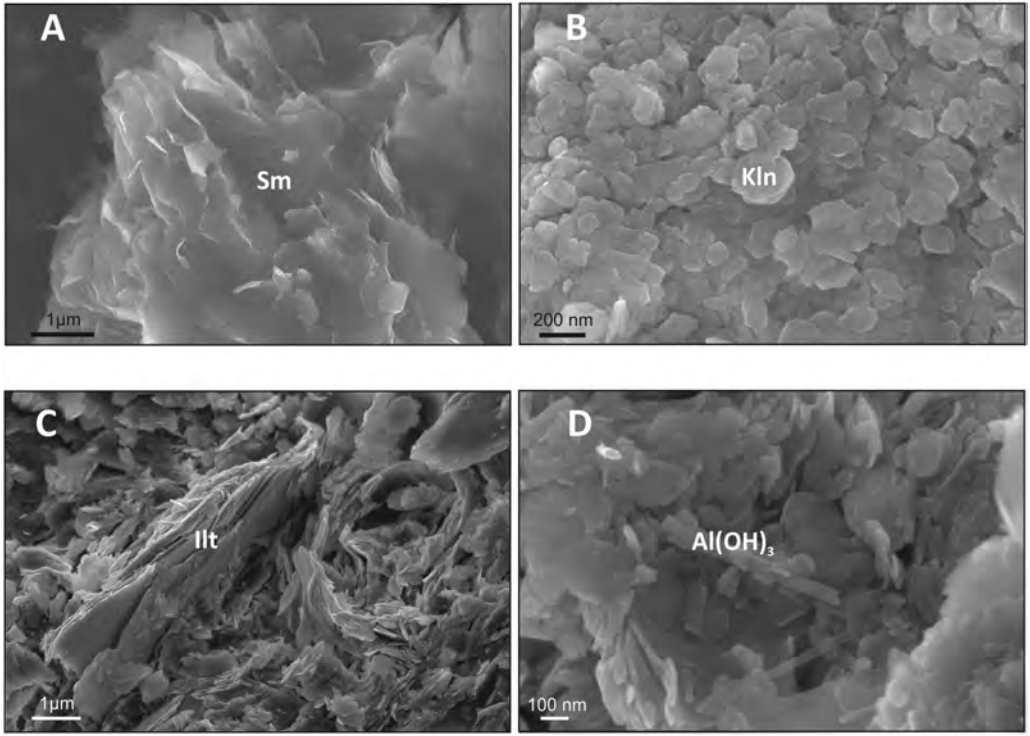


Figure 4

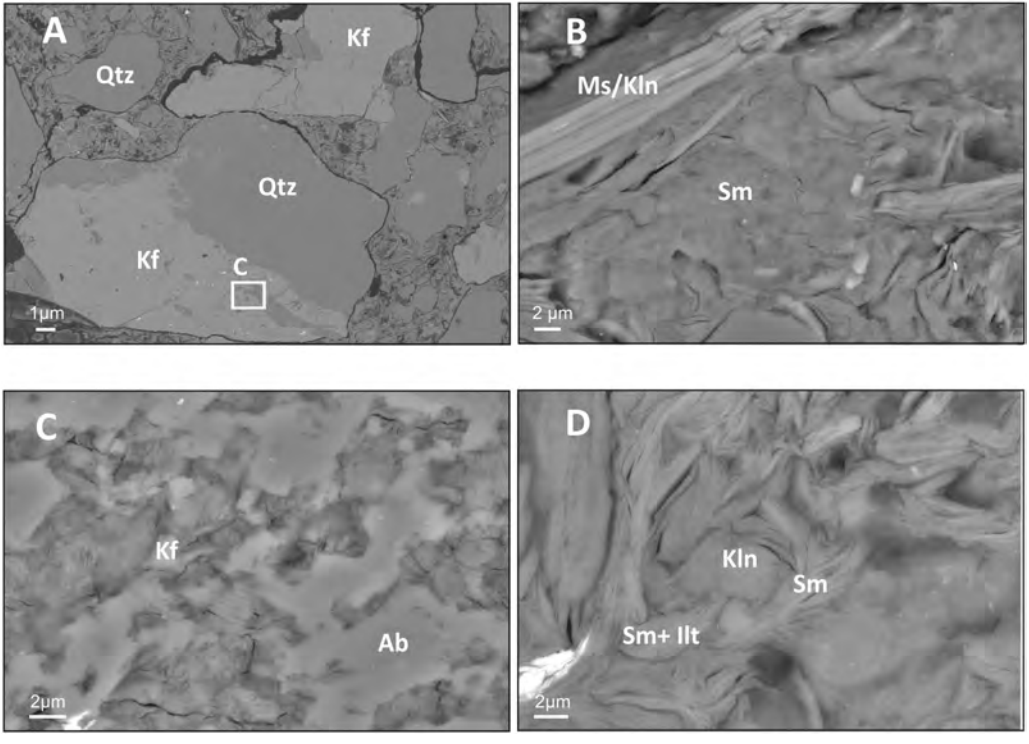


Figure 5

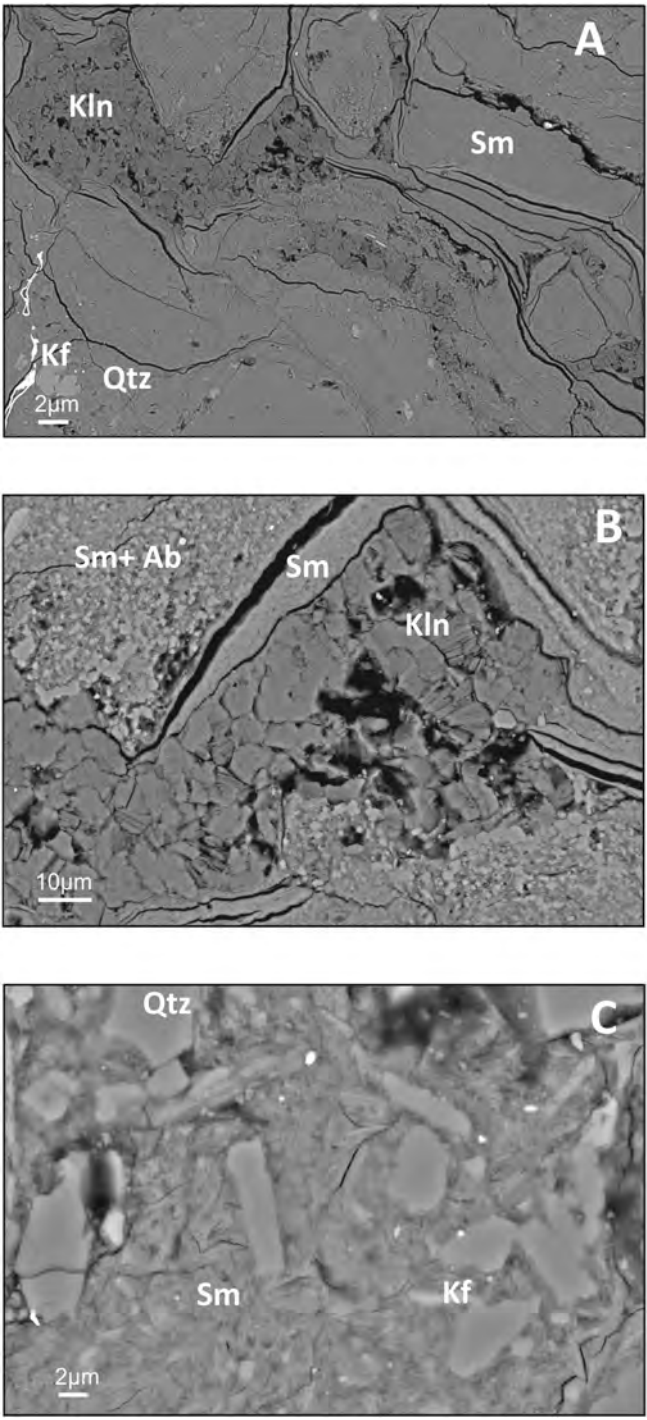


Figure 6

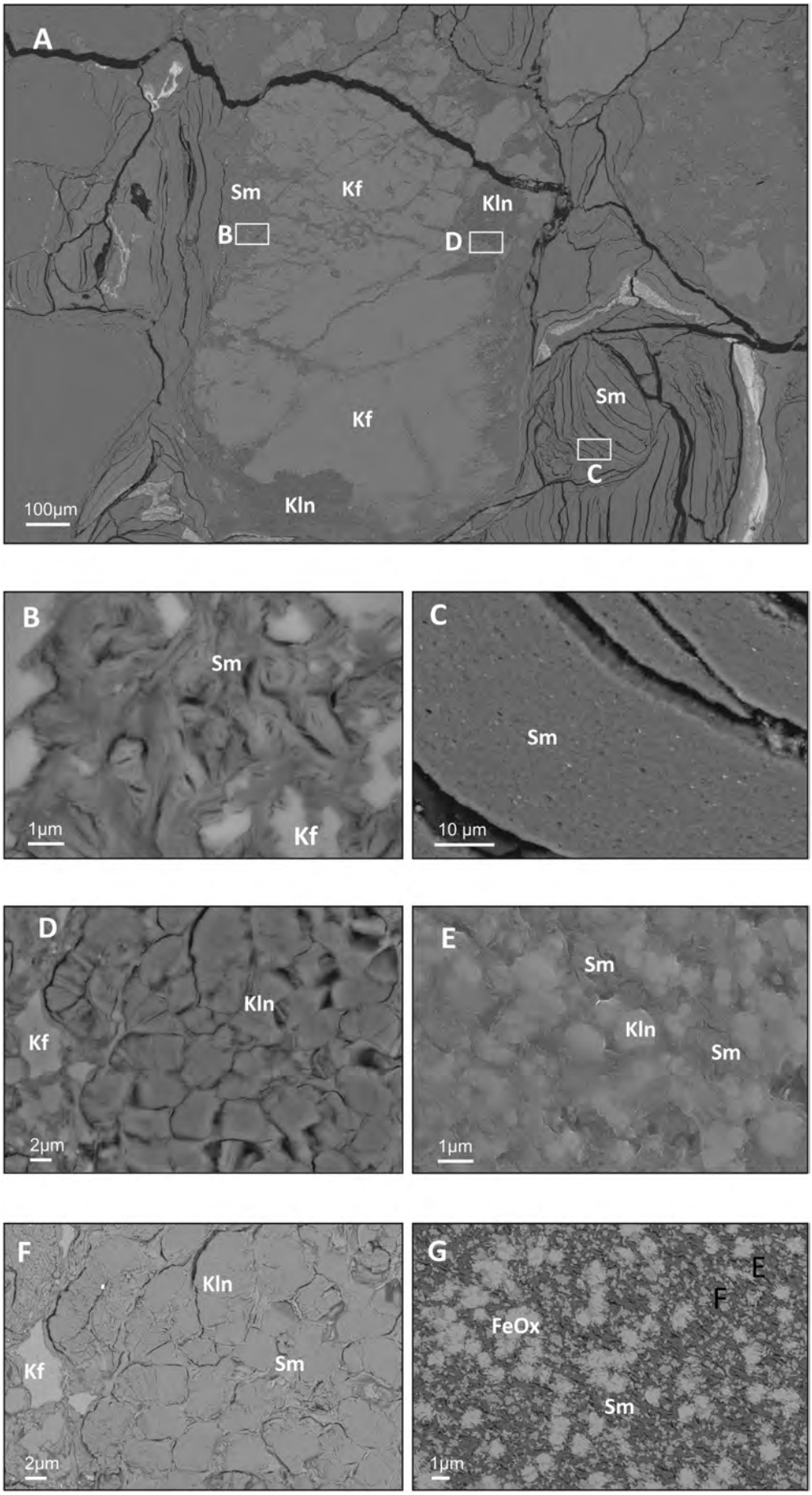
A
Sm
Kf
Kln
B
D
Sm
Kf
C
100µm
Kln
B
Sm
1µm
Kf
C
Sm
10 µm
D
Kln
Kf
2µm
E
Sm
Kln
Sm
1µm
F
Kln
Kf
Sm
2µm
G
E
F
FeOx
Sm
1µm

Figure 7

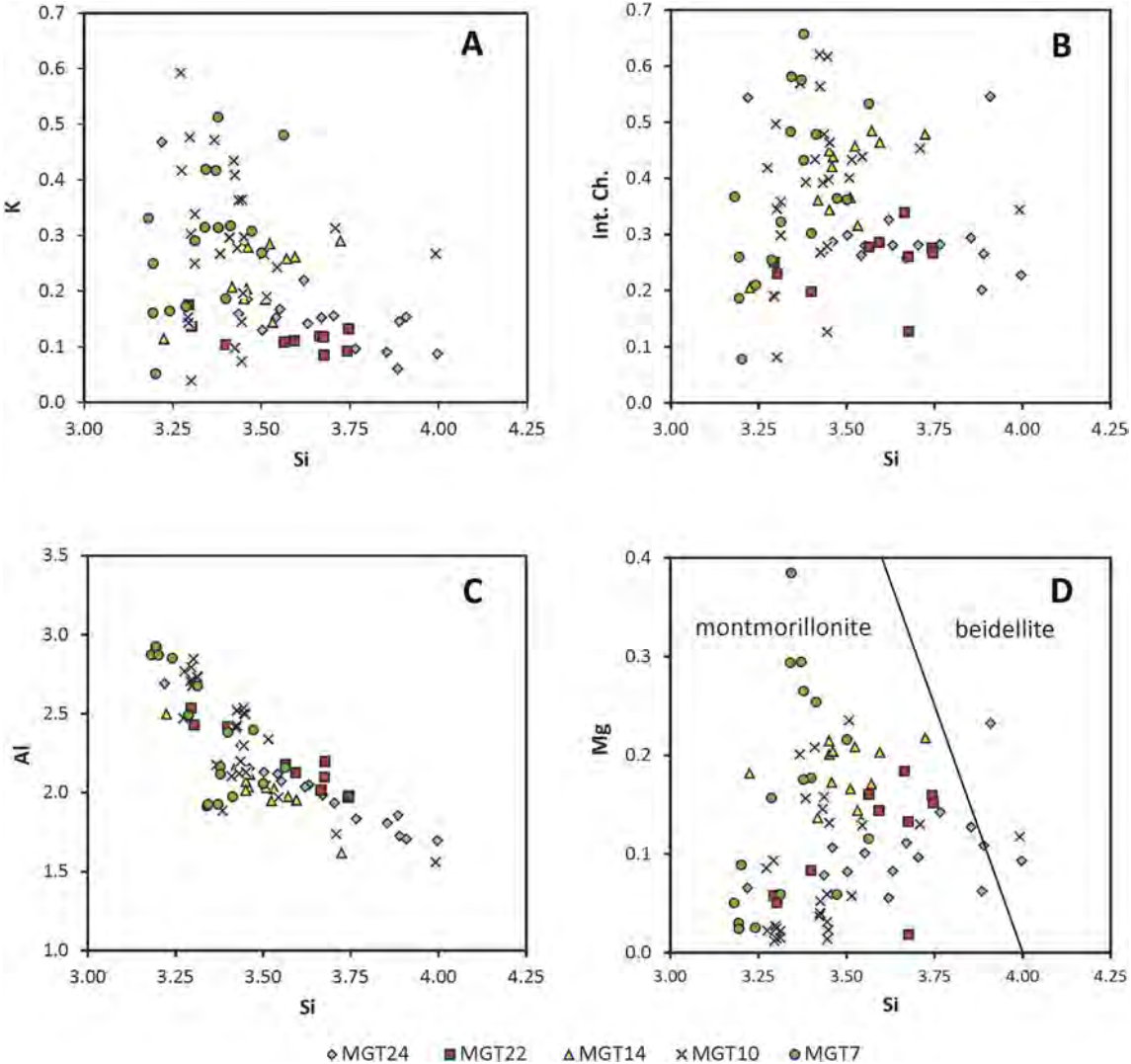
A
B
C
D
K
Int. Ch.
Al
Mg
Si
montmorillonite
beidellite
MGT24
MGT22
MGT14
MGT10
MGT7

Figure 8

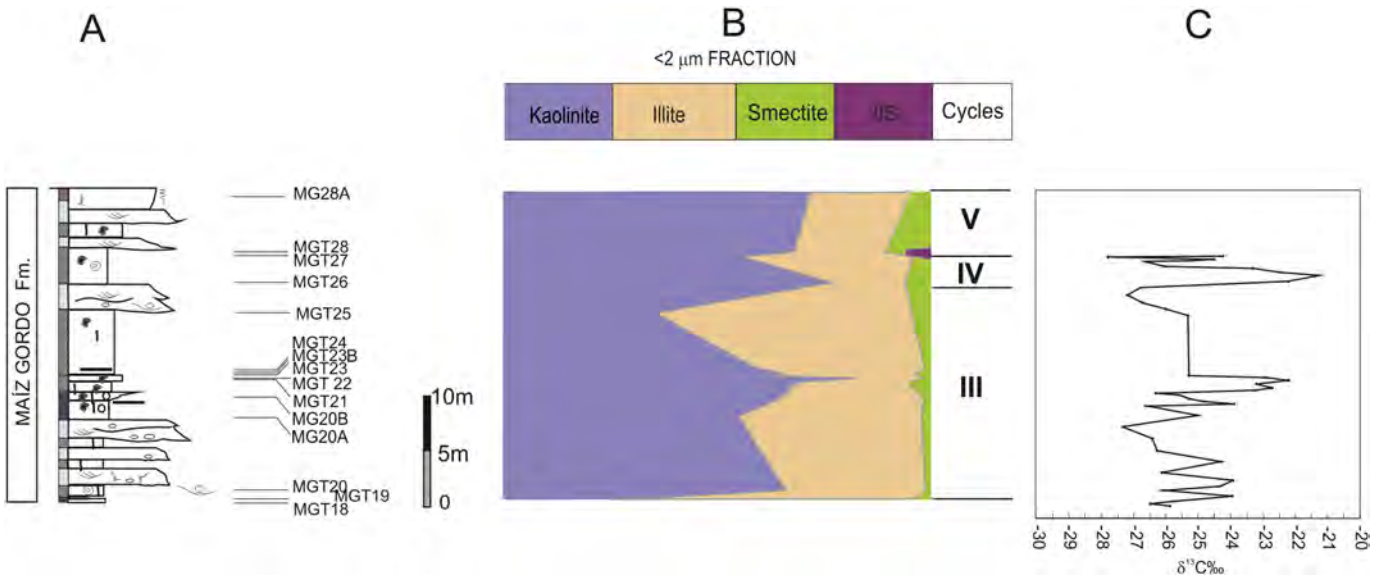
A
B
C
<2 μm FRACTION
Kaolinite
Illite
Smectite
I/S
Cycles
MAÍZ GORDO Fm.
MG28A
MGT28
MGT27
MGT26
MGT25
MGT24
MGT23B
MGT23
MGT 22
MGT21
MG20B
MG20A
MGT20
MGT19
MGT18
10m
5m
0
V
IV
III
-30
-29
-28
-27
-26
-25
-24
-23
-22
-21
-20
δ13C‰

Figure 9